Original research article

Unraveling ChR2-driven stochastic Ca^{2+} dynamics in astrocytes – A call for new interventional paradigms

Arash Moshkforoush¶, Lakshmini Balachandar¶, Carolina Moncion¶, Josue Santana, Jorge Riera Diaz*

Department of Biomedical Engineering, Florida International University

¶ Equal author contribution
* Corresponding author

Correspondence:

Jorge Riera Diaz
Department of Biomedical Engineering
Florida International University
Engineering Center
10555 West Flagler St, Miami FL 33174
Email: jrieradi@fiu.edu

Key words

Astrocyte, optogenetics, channelrhodopsin, stochastic, mathematical model, calcium dynamics

Abstract

Control of astrocytes via modulation of Ca^{2+} oscillations using techniques like optogenetics can prove to be crucial in therapeutic intervention of a variety of neurological disorders. However, a systematic study quantifying the effect of optogenetic stimulation in astrocytes is yet to be performed. Here, we propose a novel stochastic Ca^{2+}dynamics model that incorporates the light sensitive component – channelrhodopsin 2 (ChR2). Utilizing this model, we studied the effect of various pulsed light stimulation paradigms on astrocytes for select variants of ChR2 (wild type, ChETA, and ChRET/TC) in both an individual and a network of cells. Our results exhibited a consistent pattern of Ca^{2+} activity among individual cells in response to optogenetic stimulation, i.e., showing steady state regimes with increased Ca^{2+} basal level and Ca^{2+} spiking probability. Furthermore, we performed a global sensitivity analysis to assess the effect of stochasticity and variation of model parameters on astrocytic Ca^{2+} dynamics in the presence and absence of light stimulation, respectively. Results indicated that directing variants towards the first open state of the photo-cycle of ChR2 (o_1) enhances spiking activity in astrocytes during optical stimulation. Evaluation of the effect of astrocytic ChR2 expression (heterogeneity) on Ca^{2+} signaling revealed that the optimal stimulation paradigm of a network does not necessarily coincide with that of an individual cell. Simulation for ChETA-incorporated astrocytes suggest that maximal activity of a single cell reduced the spiking probability of the network of astrocytes at higher degrees of ChR2 expression efficiency due to an elevation of basal Ca^{2+} beyond physiological levels. Collectively, the framework presented in this study provides valuable information for the selection of light stimulation paradigms that elicit optimal astrocytic activity using existing ChR2 constructs, as well as aids in the engineering of future optogenetic constructs.

Author summary

Optogenetics – an avant-garde technique involves targeted delivery of light sensitive ion channels to cells. Channelrhodopsin 2 (ChR2), an algal derived light sensitive ion channel has extensively been used in neuroscience to manipulate various cell types in a guided and controlled manner. Despite being predominantly used in neurons, recent advancements have led to the expansion of the application of optogenetics in non-neuronal cell types, like astrocytes. These cells play a key role in various aspects of the central nervous system and alteration of their signaling is associated with various disorders, including epilepsy, stroke and Alzheimer's disease. Hence, invaluable information for therapeutic intervention can be obtained from using optogenetics to regulate astrocytic activity in a strategic manner. Here, we propose a novel computational model to assess astrocytic response to optogenetic stimulation which implicitly accounts for the stochastic character of Ca^{2+} signaling in this cell type. We identified light stimulation paradigms suitable for eliciting astrocytic Ca^{2+} response within physiological levels in widely-used ChR2 variants and identified highly sensitive parameters in ChR2 kinetics conducive for higher probability in Ca^{2+} spiking. Overall, the results of this model can be used to boost astrocyte light-induced behavior prediction and the development of improved future optogenetic constructs.

Glossary:

ChR - Channelrhodopsin; PM - plasma membrane; IP_3 - inositol trisphosphate; IP_3R - IP_3 receptor; CCE - capacitative calcium entry; CICR - calcium induced calcium release; SOC - store operated calcium channel; ER - endoplasmic reticulum; ATP- adenosine trisphosphate; SERCA- sarcoplasmic reticulum Ca^{2+}-ATPase; PMCA - plasma membrane Ca^{2+} ATPase; PLCδ - phospholipase C delta; SCOs - spontaneous calcium oscillations; LL - Local linearization; LHS - Latin hypercube sampling; PRCC - partial rank correlation coefficient

Introduction

Astrocytes - key players in the brain, are involved in neurovascular coupling [1-3], serve as communication elements and regulate neuronal activity via gliotransmission [4-6]. They are pivotal in housekeeping roles such as providing metabolic support to neurons [7, 8], rendering cytoarchitectonic support to the brain environment,

and maintaining carbon homeostasis which leads to the regulation of 'excitatory – inhibitory' neurotransmitter balance [9]. Astrocytes are extensively involved in the reduction of toxicity in the neuronal environment through scavenging reactive oxygen species, thereby minimizing tissue damage [10]. In the case of neurotoxic insults, they assist microglia in the *de-novo* synthesis of various cytokines and trophic factors resulting in the modulation of neuroinflammation [11-13]. Dysregulation of astrocytic function results in a multitude of brain disorders including epilepsy, stroke and Alzheimer's disease [14-20]. Hence, control of astrocytes is a powerful tool for intervening and preventing brain dysfunction. Since calcium signaling is one of the major regulatory mechanisms in astrocytes, its control can serve as a target for therapeutic intervention [21-25].

Several research groups have demonstrated the ability to elevating Ca^{2+} activity in astrocytes via electrical [26-29], mechanical [30-32] and pharmacological [33, 34] approaches. Upon electrical stimulation, astrocytes exhibit high frequency oscillations, mainly through L-type Ca^{2+} channels. However, this methodology lacks cell specificity due to potential concurrent activation of neurons and suffers low spatial resolution. Additionally, the feasibility of this method has not yet been tested *in vivo*. Mechanical stimulation, performed to mimic responses to brain injury and spreading depression [29, 35], lacks clinical feasibility. The use of pharmacological techniques for targeting these cells in the brain has been limited to basic research due to high invasiveness and low temporal resolution [36, 37]. Contrarily, optogenetics is an avant-garde minimally invasive approach, which in combination with advancements in the field of nonlinear optics [38-40], has provided a platform for genetically targeting specific cell types with high temporal and spatial precision [37, 41-43].

In spite of the recent inception of the field of optogenetics, a wide variety of optogenetic tools have been constructed, among which channelrhodopsin 2 (ChR2) has been one of the most commonly used. There exists an extensive body of literature on the biophysical characterization of ChR2 variants and their response to various light stimulation paradigms, predominantly in excitable cells [44-47]. For example, many research groups have engineered ChR2 variants for enhanced conductance, increasing recovery kinetics and capability of stimulation at lower light levels in neurons [44, 48]. ChR2 variants have also been modified to form chimeric variants for regulating responses and facilitating multiwavelength optogenetics in neurons [49]. There have been few studies

on optogenetically targeting astrocytes for specific applications [50-54], including their role in memory enhancement [55] and cortical state switching [56]. However, a holistic approach to quantify the effect of light stimulation on astrocytes has not yet been formulated, a vital step for strategic manipulation of these cells. In analyzing this effect, accounting for the stochastic nature of spontaneous calcium oscillations (SCOs) in astrocytes is imperative. The source of this stochasticity is primarily ascribed to the randomness in fluxes through IP_3R clusters and the plasma membrane (PM) [57, 58].

This paper seeks to provide a comprehensive platform via mathematical modeling to optimize light stimulation paradigms for existing optogenetic variants, yielding high astrocytic spiking rates without eliciting non-physiological behavior, and to aid the development of novel application-based constructs targeting astrocytes. To this end, we outline a novel stochastic model of astrocyte calcium dynamics with an incorporated optogenetic component - ChR2. Firstly, we quantify and evaluate the effect of different light stimulation paradigms on the Ca^{2+} dynamics of single cells expressing three existing ChR2 variants i.e. wild type, ChETA, and ChRET/TC. Secondly, to identify key features necessary for the development of prospective ChR2 constructs, we perform a global sensitivity analysis of different parameters of the single cell model to Ca^{2+} spiking rate and basal levels. Thirdly, through the incorporation of gap junctions allowing diffusion of IP_3 and Ca^{2+}, we analyze the effect of local light stimulation on the global Ca^{2+} response in a network of astrocytes homogeneously expressing ChR2. Lastly, we investigate the effect of varying degrees of heterogeneity in ChR2 expression on network-wide astrocytic Ca^{2+} spiking rate and basal level upon global light stimulation.

Materials and methods:

The biophysical model:

In this study, we present a novel biophysical model of optogenetically-modified astrocytes. The model is composed of a combination of the previously published *stochastic astrocyte model* [58, 59] and a *4-state model for ChR2* taken from Stefanescu *et al* [60] and Williams *et al* [61]. The stochastic IP_3R model is adapted from the

Li-Rinzel simplification of the De Young-Keizer model [62-64]. The 4-state ChR2 model assumes the existence of the channel in two closed states (c_1, c_2) and two open states (o_1, o_2).

(Insert Fig. 1 around here)

Figure 1 illustrates the schematic of the biophysical model of calcium dynamics of ChR2 expressing astrocytes. Cationic influx through ChR2 activation is labeled as $j_{in_{ChR2}}$. Light stimulation window is modeled as the commonly used pulse train (θ(t)) given by T (pulse period) and δ (pulse width – expressed as percentage of T). Ca^{2+} in the cytosol activates the IP_3 receptor (IP_3R) on the endoplasmic reticulum (ER) membrane, leading to an efflux of Ca^{2+} into the cytosol. Cytosolic Ca^{2+} also binds to PLC_δ (on the PM) leading to the production of IP_3 in the cytosol, which also activates IP_3R clusters. Ca^{2+} release from IP_3R leads to a further increase of IP_3R activity, also known as calcium induced calcium release (CICR). Further increase in Ca^{2+} concentration in the cytosol inactivates the release from the ER. Release of Ca^{2+} from the ER leads to capacitative calcium entry (CCE) via the transmembrane store operated calcium (SOC) channel. Uptake of Ca^{2+} via sarcoplasmic reticulum Ca^{2+}-ATPase (SERCA) pump results in the replenishment of the ER stores from the cytosol. The PM Ca^{2+} ATPase (PMCA) pump extrudes Ca^{2+} from the cytosol to the extracellular (EC) space.

Our biophysical model for a single astrocyte is composed of nine state variables, i.e. free cytosolic calcium concentration – $[Ca^{2+}]_c$, inositol triphosphate concentration – $[IP_3]$, the fraction of open inactivation IP_3R gates – h, total free Ca^{2+} concentration – c_o, fraction of ChR2 in its closed and open states – c_1, c_2, o_1,o_2, and a variable capturing temporal kinetics of conformational changes in ChR2 – s. Additive Weiner processes (σ's), which capture the stochasticity in astrocytes and ChR2 dynamics, are added as diffusion terms. A network of homogeneous/heterogeneous astrocytes was modeled by incorporation of gap junctions, J_{gj}, between the cells where the diffusion of IP_3 and Ca^{2+} were accounted for (network dynamics, Table 1). Quantification of spiking rate and Ca^{2+} basal levels were performed pre, during and post stimulus. The equations for astrocyte *'i'* in the network can be summarized by the following stochastic state-space equation:

$$d\boldsymbol{X_i} = \underbrace{\boldsymbol{f}(t,\boldsymbol{X_i},P)\,dt}_{Drift} + \underbrace{\boldsymbol{g}(P)d\omega}_{Diffusion} \quad (1)$$

where

$$\boldsymbol{X} = \begin{pmatrix} Ca^{2+}_c \\ IP_3 \\ h \\ C_0 \\ o_1 \\ o_2 \\ c_1 \\ c_2 \\ s \end{pmatrix}; \quad \boldsymbol{g} = \begin{pmatrix} \sigma_{Ca^{2+}_c} \\ \sigma_{IP_3} \\ \sigma_h \\ \sigma_{C_0} \\ \sigma_{o_1} \\ \sigma_{o_2} \\ \sigma_{c_1} \\ \sigma_{c_2} \\ \sigma_s \end{pmatrix}; \quad (1.1)$$

P denotes the parameters of the model, summarized in Table 1, and components of the $\boldsymbol{f}$ vector will be described in detail. We have previously estimated the variance of the Weiner processes for IP_3, Ca_c , h and c_o, using the local linearization (LL) filter [59, 65] (Weiner processes, Table 1). Potential stochasticity in ChR2 dynamics is included in the model using constant Weiner processes and will be explored in later sections.

The dynamics of free cytosolic calcium concentration is given by

$$d[Ca^{2+}]_{c_i} = \left(\lambda(v_{Rel} - v_{SERCA}) + \varepsilon(j_{in} + v_{CCE} - v_{out} + j_{in,ChR2}) - J_{gj_{Ca_i}}\right)dt + \sigma_{Ca^{2+}}dw_{Ca^{2+}} \quad (2)$$

$$J_{gj_{Ca_i}} = \sum_k D_{Ca}([Ca]_{c_i} - [Ca]_{c_k}) \quad (2.1)$$

Where $J_{gj_{Ca_i}}$ is the gap junctional flux of Ca^{2+} flowing from astrocyte 'i' to its neighboring astrocytes (indicated by index k). The efflux of Ca^{2+} from the ER to the cytosol via the IP_3R is described by

$$v_{Rel} = \alpha_1(v_1 m_\infty^3 h_i^3 + v_2)([Ca^{2+}]_{ER} - [Ca^{2+}]_{c_i}) \quad (2.2)$$

where calcium in the ER is given by

$$[Ca^{2+}]_{ER} = \frac{(c_{o_i} - [Ca^{2+}]_{c_i})}{\alpha_1} \quad (2.3)$$

The steady state profile of the open activation IP_3R gates is

$$m_\infty = \frac{[IP_3]_i[Ca^{2+}]_{c_i}}{([IP_3]_i + d_1)([Ca^{2+}]_{c_i} + d_5)} \quad (2.4)$$

A hill-type kinetic model describing the SERCA pumping is given by

$$v_{SERCA} = V_{SERCA}\frac{\left([Ca^{2+}]_{c_i}\right)^2}{\left([Ca^{2+}]_{c_i}\right)^2 + (K_p)^2} \quad (2.5)$$

The CCE effect is described as a phenomenological model using the following equation

$$v_{CCE} = \frac{x_{CCE}(h_{CCE})^2}{\left(\frac{c_{o_i} - [Ca^{2+}]_{c_i}}{c_1}\right)^2 + (h_{CCE})^2} \quad (2.6)$$

Ca^{2+} extrusion across the PM via PMCA is given by

$$v_{out} = k_{out}[Ca^{2+}]_{c_i} \quad (2.7)$$

IP_3 changes in astrocytes mediated by $PLC_{\delta 1}$ and intercellular diffusion is described as:

$$d[IP_3]_i = \left(X_{IP_3} + PLC_{\delta 1} - K_{IP_3}[IP_3]_i - J_{gj_{IP_{3i}}}\right)dt + \sigma_{IP3}dw_{IP3} \quad (3)$$

where X_{IP_3} denotes the basal level of IP_3 production (μM/s) from fluctuations in the action of receptor-agonists over G-protein-coupled receptors, and $J_{gj_{IP_{3i}}}$ is the gap junctional flux of IP_3 flowing from astrocyte 'i' to its neighboring astrocytes, defined as:

$$J_{gj_{IP_{3i}}} = \sum_K D_{IP_3}([IP_3]_i - [IP_3]_k) \quad (3.1)$$

$PLC_{\delta 1}$ activity is described as the Hill's kinetic model as

$$PLC_{\delta_1} = v_\delta \frac{\left([Ca^{2+}]_{c_i}\right)^2}{\left([Ca^{2+}]_{c_i}\right)^2 + (K_{\delta Ca})^2} \quad (3.2)$$

Dynamics of the fraction of open inactivation IP_3R inactivation gates is given by

$$dh_i = [\alpha_h(1 - h_i) - \beta_h h_i]dt + \sigma_h dw_h \quad (4)$$

where the opening (α_h) and closing rates (β_h) rates are

$$\alpha_h = \frac{ad_2([IP_3]_i + d_1)}{[IP_3]_i + d_3} \quad (4.1)$$

$$\beta_h = a[Ca^{2+}]_{c_i} \quad (4.2)$$

The total free $[Ca^{2+}]$ in the cell ($[Ca^{2+}]_c + [Ca^{2+}]_{ER}$) is modeled as

178 $$dc_{0_i} = (\varepsilon(j_{in} + v_{CCE} - v_{out} + j_{in,ChR2}) - J_{Ca_{c_i}})dt + \sigma_{Co} dw_{Co} \quad (5)$$

179 The open and closed gating dynamics of ChR2 are given by equations 5-8, as

180 $$do_{1_i} = (p_1 s_i c_{1_i} - (G_{d_1} + e_{12}) o_{1i} + e_{21} o_{2_i}) dt + \sigma_{O_1} dw_{O_1} \quad (6)$$

181 $$do_{2_i} = (p_2 s_i c_{2_i} + e_{12} o_{1_i} - (G_{d_2} + e_{21}) o_{2_i}) dt + \sigma_{O_2} dw_{O_2} \quad (7)$$

182 $$dc_{2_i} = (G_{d_2} O_{2_i} - (P_2 s_i + G_r) c_{2_i}) dt + \sigma_{c_2} dw_{c_2} \quad (8)$$

183 $$ds_i = \left(\frac{(S_0(\theta) - s_i)}{\tau_{ChR2}}\right) dt + \sigma_S dw_S \quad (9)$$

184 where $\theta(t)$ describes the laser stimulus paradigm as a pulse train, and:

185 $$S_0(\theta) = 0.5(1 + \tanh(120(\theta - 0.1))) \quad (9.1)$$

186 The existence of ChR2 in various states should satisfy the following algebraic condition:

187 $$c_1 + c_2 + o_1 + o_2 = 1 \quad (10)$$

188 The current generated by cationic influx through ChR2 is given by

189 $$I_{ChR2} = g_1 A_m G(V_m)(o_{1_i} + \gamma o_{2_i})(V_m - E_{ChR2}) \quad (11)$$

190 where $$G(V_m) = \frac{\left(10.6408 - 14.6408 exp^{-\left(\frac{V_m}{42.7671}\right)}\right)}{V_m} \quad (11.1)$$

191 The resultant flux through ChR2 is

192 $$j_{in,ChR2} = \frac{I_{ChR2}}{F vol_{cyt} z_{Ca^{2+}}} \quad (11.2)$$

193 The diffusion term in equation 1 implies solving of the state-space system as an integrated model. In a
194 deterministic system, due to lack of feedback from Ca^{2+} dynamics into that of ChR2, the dynamics of ChR2 can
195 be solved independently. The model was implemented in MATLAB 2018a (Mathworks Inc.) and was numerically

196 solved using the LL method [59] with an integration step size of $\Delta t = 0.1$ ms. A listing of all parameters and their
197 descriptions can be found in Tables 1 and 2.

198 ***Light stimulation paradigm***

199 In all simulations performed in this study, laser stimulus was modeled as a square wave pulse train with period
200 T, pulse width δ (expressed as a percentage of T), and unit pulse amplitude. This paradigm is employed to evaluate
201 the effect of light on astrocytic activity, in both individual and a network of gap junction connected astrocytes.

202 ***Sensitivity Analysis***

203 A global sensitivity analysis was performed to assess the sensitivity of SCOs to stochastic noise, without light
204 stimulation. The Latin hypercube sampling (LHS) method with uniform distribution was used to select parameter
205 sets for testing and solving the system [66, 67]. Variance of each of the Weiner processes was varied between a
206 lower and an upper bound (state variable variances, Table 3), and the partial rank correlation coefficient (PRCC)
207 analysis was performed. 95% confidence interval was chosen for statistical significance. A similar global
208 sensitivity analysis was performed to quantify the sensitivity of the Ca^{2+} response to the parameters of ChR2,
209 during light stimulation. Parameter sets accommodating for ranges across parameters were chosen by the LHS
210 method with uniform distribution and the PRCCs were computed with respect to the spiking rate and Ca^{2+} basal
211 level in the astrocyte.

212 **Results:**

213 **Response of ChR2 variants to light stimulation**

214 **(Insert Figure 2 around here)**

215 Figure 2 shows a representative simulation of the response to light stimulation of single astrocytes expressing
216 four ChR2 variants - wt1, wt2, ChETA, and ChRET/TC (refer to Table 2 for their gating parameters and
217 conductance). The light stimulation paradigm employed had T = 1s, δ = 20% with a unit pulse amplitude. Within
218 the 20-minute window of simulation, the laser stimulus was applied to the astrocyte from 4-12 minutes. Upon

light stimulation (panels A-D), the dynamic system shows increases in [IP_3], [Ca^{2+}] and [c_o] across ChR2 variants in the order of wt1<wt2<ChETA<ChRET/TC, while the IP_3R gating variable (h) shows a decrease in the order of wt1>wt2>ChETA> ChRET/TC. In addition, as compared to the pre and the post light stimulus phases, there is an increase in basal Ca^{2+} levels during light stimulation. The ChR2 gating dynamics (panels E-H) indicate that before light stimulation there is a maximum probability of existence of the channel in the c_1 state. However, upon stimulation, different ChR2 variants show that the dynamic system proceeds to the other states (o_1, o_2 and c_2), with them showing differing gating dynamics.

Response of a ChETA-expressing astrocyte to various light stimulation paradigms

(Insert Figure 3 around here)

Figure 3 shows the effect of stimulation paradigms on the mean spiking rate and the steady state Ca^{2+} basal level in astrocytes expressing ChETA (for other ChR2 variants refer to Figures S1-3). Laser parameters (Figure 1) - T and δ were varied between 1-5 seconds and 0-100% of T, respectively. Figure 3A shows a histogram of all Ca^{2+} spikes pre and during light stimulation. To exclude minor irrelevant Ca^{2+} fluctuations, a cutoff prominence (dashed line – 350 nM) was chosen for spiking rate calculations. The cutoff concentration was chosen based on the bimodal distribution of the spiking rate histogram, ensuring that only spikes in the larger mode were chosen and those related to the 1/f noise were excluded from the analysis.

For each combination of T and δ, 10 trials were performed for 40 minutes, with the light stimulation starting at 50 seconds until the end of the simulation (indicated by the grey window and the blue bar). Once the Ca^{2+} baseline reached a steady profile (indicated by the orange region), the mean spiking rate across trials and mean basal levels were calculated for each stimulation paradigm. The T-δ heat (color) maps, useful to determine optimal Ca^{2+} signaling behavior in astrocytes exposed to a variety of T and δ combinations, are shown in Figure 3B and C for Ca^{2+} baseline and Ca^{2+} spiking, respectively. Results indicate that in the physiologically acceptable ranges chosen for T and δ (Ca^{2+} basal levels higher than reported physiological values are separated by the dashed white trace in panel B), there are regions of increased astrocytic Ca^{2+} spiking activity (red regions in Figure 3C). Three

representative traces from regions with low, intermediate and high astrocytic Ca^{2+} spiking activity with physiological Ca^{2+} basal levels are depicted in Figure 3D.

Sensitivity of the astrocytic Ca^{2+} response to system state variables and ChR2 parameters

(Insert Figure 4 around here)

In Figure 4, a global sensitivity analysis was performed to evaluate the Ca^{2+} response of astrocytes (i.e. the spiking rate and steady basal level) to variations in the stochastic noise variances of the state variables (without light stimulus) as well as to variations in the parameters of ChR2 (during light stimulation). To generate Figure 4A, simulations were performed for 10 minutes, for 10 trials without light stimulation. The range of the variances (σ's) were chosen between 0 and 0.10 (state variable variances, Table 3). The LHS method with uniform distribution was used to choose 500 parameter sets for simulations. The PRCC of the variances of the Wiener processes with respect to the mean Ca^{2+} spiking rates, along with the corresponding p-values were computed. As seen, SCOs are highly sensitive (indicated by *) to the variances in the order of $\sigma_{Ca_c} > \sigma_h > \sigma_{IP_3} > \sigma_{C_o} > \sigma_{O_1}$; however, the contributions of σ_{O_2} and σ_{C_2} were not significant.

Figure 4B shows the sensitivity of Ca^{2+} activity to parameters of ChR2 during light stimulation with the paradigm shown in Figure 3D, trace 1 (T = 4.5s and δ = 30%). Similar to the analysis in Figure 3A, the cutoff prominence of the peaks counted was set to 350 nM to exclude 1/f noise related Ca^{2+} spikes. The range of each parameter was chosen such that the four ChR2 variants were encompassed in it (ChR2 parameters, Table 3). 1000 parameter sets were chosen using the LHS method with uniform distribution. For each parameter set, 10 trial simulations were performed, each with a duration of 40 minutes, and the respective Ca^{2+} spiking rate and steady basal levels were calculated. Light stimulation was initiated at 50 seconds and continued for the duration of simulation. The PRCCs were computed and plotted for each of the ChR2 parameters evaluated in this study (Figure 4B). The results indicate that the parameters e_{12}, e_{21} and g_1 are statistically significant at a 95% confidence interval, for both, the Ca^{2+} spiking rate and basal level. While e_{12}, G_{d1} and G_{d2} are negatively correlated to the Ca^{2+} response with respect to both the spiking rate and basal level, e_{21}, p_2 and g_1 are positively correlated. Parameters τ_{ChR2} and γ are

267 statistically significant and positively correlated to the Ca^{2+} response with respect to the basal level and spiking
268 rate, respectively.

269 **Network-wide response of homogenously ChR2-expressing astrocytes to light stimulation**

270 **(Insert Figure 5 around here)**

271 Figure 5 shows the effect of light stimulation on a network of 10x10 astrocytes homogenously expressing the
272 ChR2 variant - ChETA. Astrocytes are connected to each other in all orientations, i.e., horizontal, vertical and
273 diagonal directions. Light stimulation was performed with T = 2s and δ = 15% and between 12 – 25 minutes
274 (indicated by the grey shaded region, blue bar). The spiking rate in response to the light stimulation was computed
275 as a network-wide behavior throughout the total period. Figure 5A shows a histogram of all Ca^{2+} spikes, pre and
276 during light stimulation, revealing also bimodal distributions. Similar to previous simulations, to exclude
277 irrelevant Ca^{2+} fluctuations due to 1/f noise, a cutoff prominence (dashed line – 350 nM) was chosen for spiking
278 rate calculations. A representative trace of the cytosolic Ca^{2+} is shown in Figure 5B, with the properties of the
279 trace used for quantification, i.e. peak prominence and peaks detected. The grey shaded region represents the time
280 period during which laser stimulation was performed. Network-wide responses to light stimulation, quantified by
281 the mean spiking rate for each cell are shown as heat maps, which were calculated for the pre, during and post
282 light stimulation phases (Figure 5C). The network Ca^{2+} baselines at three specific time instances within the pre,
283 during and post stimulus phases, are shown in Figure 5D (for the full video, refer to supplementary video S1).
284 The spatial arrangement of astrocytes and the subnetwork of astrocytes being stimulated are shown in Figure 5E.
285 Astrocytes along the diagonal (red) are labeled 1 through 6. The Ca^{2+} activity traces of each cell along the diagonal
286 are shown in Figure 5F. Results indicate that there are SCOs across the network, prior to light stimulation, while
287 during stimulation, the astrocytic Ca^{2+} spiking rate is maximum in and around the area of light stimulation. Post
288 light stimulation, the activity is dispersed throughout the network and lasts for long periods of time (Figure 5 B,
289 C and F). Inspection of Ca^{2+} activity traces of various cells across a diagonal with increasing distance from the

center of the light stimulation area indicates that there is a decrease in Ca^{2+} spiking rate (Figure 5F). This suggests that there is a propagation of the Ca^{2+} spiking probability resulting in a network-wide effect on Ca^{2+} dynamics.

Effect of ChETA-expression heterogeneity on network-wide light stimulation

(Insert Figure 6 around here)

Figure 6 shows the effect of light stimulation on a network of 5x5 astrocytes with varying degrees of expression of ChETA. The astrocytes are connected in all directions via gap junctions. For each expression level, five random distributions of ChR2 expressing astrocytes were generated, and simulations were performed (15 minutes, 5 trials). Light stimulation was performed from 50 seconds until the end of the simulation. Once Ca^{2+} baseline reached a steady profile, the mean and standard deviation of spiking rates and Ca^{2+} basal levels were computed. Figures 6A ($T = 5s$, $\delta = 40\%$) and 6B ($T = 2.5s$, $\delta = 10\%$) show an increase in Ca^{2+} basal levels and spiking rate in the network, corresponding to increases in ChR2 expression levels. It is to be noted that in the abovementioned light stimulation paradigms, the Ca^{2+} basal levels are within physiological levels (indicated by dashed line). Although Figure 6C ($T = 2s$, $\delta = 40\%$) showed an increase in the Ca^{2+} baseline when the ChR2 expression was increased, there is an overshoot beyond physiological levels at the 80 and 100 % expression levels. Ca^{2+} spiking rate, on the other hand, shows an initial increase until 50% expression level, post which displayed a declining trend.

Discussion

We developed a novel stochastic model to assess the effect of light stimulation on the Ca^{2+} dynamics in astrocytes expressing the widely used opsin - ChR2. We used three ChR2 variants - wild type, ChETA, and ChRET/TC. The proposed framework can further be adopted for investigating other opsins. Our model accounts for major intracellular calcium signaling pathways as well as light-activated cationic influx through ChR2. We studied light-induced Ca^{2+} responses in both a single astrocyte and a network of homogenously/heterogeneously ChR2

expressing astrocytes. We identified favorable light stimulation paradigms for the abovementioned ChR2 variants which result in maximal spiking rates in astrocytic Ca^{2+} activity within physiological Ca^{2+} basal levels. We also quantified the sensitivity of the model output to changes in the regulation kinetics and in the conductance of ChR2. The model presented in this study provides an insight into stimulation paradigms ideal for controlling astrocytic Ca^{2+} activity and offers geneticists an efficient theoretical framework for the design of new variants.

Results show that calcium dynamics in astrocytes, as seen in experimental studies [51], can be heavily regulated by light-induced activation of ChR2 (Figures 2-3 and S1-3). According to our findings, all ChR2 variants studied in this paper showed similar profiles of activity in response to different laser pulse specifications (Figure 3, S1-3). The profiles displayed common regions of high spiking rate (point 3, Figure 3C), as well as regions with intermediate (point 2, Figure 3C) and low activity (point 1, Figure 3C). Also, with the increase in δ, there is a consistent increase in the basal level observed at any given T. This drastic variability of astrocytic model response to varying stimulation paradigms emphasizes the importance of choosing 'ideal' T and δ for desired astrocytic activity in future studies. A wrong selection of these two parameters could prompt these cells to an unhealthy Ca^{2+} signaling regime.

Global sensitivity analysis (Figure 4A) indicates that SCOs are significantly dependent on the stochasticity of IP_3 dynamics, PM fluxes and the o_1 state of ChR2. Similar dependencies to IP_3 receptor activity and membrane fluxes have been shown by us [59] and in a recent study by Ding *et al* [57]. Although the source of stochasticity in ChR2 dynamics is yet to be investigated, we hypothesize that potential protein thermal noise and fluctuations in light intensity due to photon migration dynamics may play a role. Figure 4B indicates that the kinetics of ChR2 significantly affect Ca^{2+} spiking rate and basal level. As a general trend, intuitively, directing ChR2 to the open states (o_1 and o_2) from the closed states (c_1 and c_2) leads to an increase in astrocytic activity in response to light stimulation. For instance, decreasing G_{d_1} and G_{d_2} facilitates the existence of ChR2 in the open states as they are negatively correlated to the basal level and spiking rate. Also, increase in p_2 drives the system to the open state. Similarly, increase in the conductance of ChR2 results in enhanced ionic influx into the cell, thereby elevating

337 both spiking rate and basal levels of calcium. However, less intuitively, increased astrocytic activity occurs when
338 ChR2 exists in the o_1 state as compared to the o_2 state. This can be observed, as an increase in e_{21} and decrease in
339 e_{12} led to the existence of ChR2 in o_1 state (see Figure 1 inset). Collectively, our results suggest that for the light
340 stimulation paradigm used in our global sensitivity analysis, maximal astrocytic activity can be achieved when
341 ChR2 is directed towards the o_1 state, which can be used for future development of ChR2 variants.

342 An important aspect in experimental optogenetics is ChR2 expression levels (e.g., transduction efficiency). While
343 incorporating genetic material into the cell, heterogeneity in the degree of expression might occur [68, 69]. Model
344 results suggest that network-wide Ca^{2+} response in astrocytes to light stimulation depends heavily not only on the
345 expanse of stimulation and specification of the paradigm, but also on the degree of heterogeneity (Figures 5, 6,
346 S1-3). We observed the propagation of the probability of Ca^{2+} spiking in response to local light stimulus in a
347 network of homogeneously ChR2 - expressing astrocytes (efficiency of 100%, Figure 5). In heterogeneously
348 ChR2 – expressing astrocytes subjected to a given network-wide stimulus paradigm, differing degrees of
349 heterogeneity resulted in varying degrees of Ca^{2+} spiking and basal levels (Figure 6). The expected increase in
350 the Ca^{2+} spiking rate with the increase in the fraction of ChR2 expression was observed in stimulation paradigms
351 corresponding to points 1 and 2 in Figure 3 (Figure 6A and B). However, notably, due to saturation of astrocytic
352 Ca^{2+} signaling, i.e., elevation of the Ca^{2+} baseline beyond physiological levels, there is a counteracting effect on
353 Ca^{2+} spiking rate when expression is increased (Figure 6C at 80 and 100%). This indicates that design of
354 experiments for stimulation of a network of genetically altered astrocytes cannot be solely based upon
355 observations from single cells, as other factors like ChR2 expression levels and the specific stimulation design
356 (T, δ) play a significant role.

357 The model presented in this paper aimed at studying the effect of light stimulation on Ca^{2+} dynamics in
358 optogenetically-enabled astrocytes. The model does not include the dynamics of other major ionic species crucial
359 in the function of these cells. Furthermore, membrane electric potential dynamics are not included in the current
360 model, and hence voltage gated calcium channels have not been incorporated. This modeling approach can be
361 applied to other ChR2 variants upon availability of quantified parameters. We sought to provide a minimalistic

theoretical framework which can readily be employed by researchers for the investigation of light induced Ca^{2+} responses in astrocytes. Combination of the presented model with more detailed models as in Savtchenko *et al* [70] and Lallouette *et al* [71] where exhaustive geometry and dynamics of various ionic species important for astrocytic Ca^{2+} signaling are accounted for, can enhance our understanding of the intricacies of the behavior of these cells and their response to light.

Acknowledgments

This study was supported by the National Institutes of Health (1R56NS094784-01A), Wallace Coulter Foundation – BME SEED grant – Florida International University (FIU), and Dissertation Year Fellowship (DYF) from the University Graduate School at FIU (Arash Moshkforoush). The authors would like to sincerely thank Dr. James Schummers, Dr. Nikolaos Tsoukias, Dr. Rita Alevriadou, Mr. Ramkrishnan Krishnan, and Mr. Ricardo Siu for insightful discussions.

Author contributions

Model development: AM LB CM JS JR. Analysis/discussion of results: CM AM LB JR. Literature review: LB AM CM. Manuscript writing: LB AM CM JR.

Table 1. Astrocyte Model Parameters

	Parameter	*Value*	*Unit*	*Description*	*Source*
IP_3 Dynamics	v_δ	0.15	μM/s	Maximum rate of IP_3 production (PLC_δ)	[58, 59]
	$K_\delta Ca$	0.56	μM	Half saturation constant of Ca^{2+} resulting from IP_3 synthesis (PLC_δ)	[58, 59]
	K_{IP_3}	1.25	s^{-1}	IP_3 degradation rate	[58, 59, 72]
	X_{IP_3}	0.14	μM/s	Basal level of cytosolic IP_3 production	[58, 59]
Ca^{2+} Dynamics	x_{CCE}	0.01	μM/s	Maximum rate of activation dependent on Ca^{2+} (CCE) influx (phenomenological value)	[58, 59, 73]
	h_{CCE}	10	μM	Half-inactivation constant for CCE influx	[58, 59, 73]
	α_1	0.19	~	Volume ratio between ER and cytosol	[58, 59]
	v_{SERCA}	0.90	μM/s	Maximum rate constant of SERCA pump	[58, 59, 74]
	K_{p}	0.10	μM	Ca^{2+} sensitivity of the SERCA pump	[58, 59, 75-77]
	d_1	0.13	μM	Dissociation constant for IP_3 (IP_3R)	[58, 59, 63]
	d_5	0.08	μM	Ca^{2+} activation constant (IP_3R)	[58, 59, 63]
	v_1	6	s^{-1}	Ligand-operated IP_3R channel flux constant	[58, 59, 74, 77]
	v_2	0.11	s^{-1}	Ca^{2+} passive leakage flux constant	[58, 59, 74, 77]
	k_{out}	0.50	s^{-1}	Rate constant of Ca^{2+} extrusion	[58, 59]
	λ	1	~	Time scaling factor	[58, 59]
	ε	0.01	~	Ratio of PM to ER membrane surface area	[58, 59, 63]

	j_{in}	0.04	μM/s	Passive leakage	[58, 59]
	v_m	-70	mV	Membrane voltage	
	vol_{cyt}	10^{-12}	L	Volume of the cytosol, assuming spherical cell	[78]
	A_m	4.83×10^{-6}	cm^2	Surface area of the astrocyte membrane (calculated using vol_{cyt} and assuming spherical cell shape)	~
	F	9.65×10^4	C/mol	Faraday's constant	~
	z_{Ca}	2	~	Valence of Ca^{2+}	~
Gating Parameters	a	0.20	$(\mu Ms)^{-1}$	Rate constant for Ca^{2+} binding in IP_3 inhibitory site	[58, 59, 63]
	d_2	1.05	μM	Dissociation constant for Ca^{2+} inhibition (IP_3R)	[58, 59, 63]
	d_3	0.94	μM	Dissociation constant for IP_3 (IP_3R)	[58, 59, 63]
Network Dynamics	D_{IP_3}	1	s^{-1}	Rate of IP_3 diffusion	[77]
	$D_{Ca^{2+}}$	0.01	s^{-1}	Rate of Ca^{2+} diffusion	[77]
Weiner Processes	σ_{IP_3}	0.02	$s^{-1/2}$	Variance of Wiener process of IP_3	[58, 59]
	$\sigma_{Ca^{2+}}$	0.01	$s^{-1/2}$	Variance of Wiener process of Ca_c	[58, 59]
	σ_h	0.07	$s^{-1/2}$	Variance of Wiener process of h	[58, 59]
	σ_{c_o}	0.01	$s^{-1/2}$	Variance of Wiener process of c_o	[58, 59]
	σ_{o_1}	0.02	$s^{-1/2}$	Variance of Wiener process of o_1	Model est.
	σ_{o_2}	0.02	$s^{-1/2}$	Variance of Wiener process of o_2	Model est.
	σ_{c_2}	0.02	$s^{-1/2}$	Variance of Wiener process of c_2	Model est.
	σ_s	0	$s^{-1/2}$	Variance of Wiener process of s	Model est.

Table 2. ChR2 4-State Model Parameters

Parameter	*ChR2 Variant*	*Value*	*Unit*	*Description*	*Source*
p_1	**ChRwt**	0.06	ms^{-1}	Maximum excitation rate of c_1	[44, 48, 60]
	ChRwt2	0.12			
	ChETA	0.07			
	ChRET/TC	0.13			
G_{d_1}	**ChRwt**	0 46	ms^{-1}	Rate constant for the o_1 to c_1 transition	[44, 48, 60]
	ChRwt2	0.01			
	ChETA	0.01			
	ChRET/TC	0.01			
e_{12}	**ChRwt**	0.20	ms^{-1}	Rate constant for the o_1 to o_2 transition	[44, 48, 60]
	ChRwt2	4.38			
	ChETA	10.51			
	ChRET/TC	16.11			
e_{21}	**ChRwt**	0.01	ms^{-1}	Rate constant for the o_2 to o_1 transition	[44, 48, 60]
	ChRwt2	1.60			
	ChETA	0.01			
	ChRET/TC	1.09			
p_2	**ChRwt**	0.06	ms^{-1}	Maximum excitation rate of c_2	[44, 48, 60]
	ChRwt2	0.01			
	ChETA	0.06			
	ChRET/TC	0.02			
G_{d_2}	**ChRwt**	0.07	ms^{-1}	Rate constant for the o_2 to c_2 transition	[44, 48, 60]
	ChRwt2	0.12			

	ChETA	0.15			
	ChRET/TC	0.13			
G_r	**ChRwt**	9.35×10^{-5}	ms^{-1}	Recovery rate of the c_1 state after light pulse is turned off	[44, 48, 60]
	ChRwt2	9.35×10^{-5}			
	ChETA	1×10^{-3}			
	ChRET/TC	3.85×10^{-4}			
τ_{ChR2}	**ChRwt**	6.32	ms^{-1}	Activation time of the ChR2 ion channel	[44, 48, 60]
	ChRwt2	0.51			
	ChETA	1.59			
	ChRET/TC	0.36			
g_1	**ChRwt**	0.03	mS/cm^2	Maximum conductance of the ChR2 ion channel in the o_1 state	[44, 48, 60]
	ChRwt2	0.02			
	ChETA	0.01			
	ChRET/TC	0.02			
γ	**ChRwt**	0.11	~	Ratio of maximum conductance of the ChR2 ion channel in the o_2 and o_1 state $\left(\frac{g_2}{g_1}\right)$	[44, 48, 60]
	ChRwt2	0.10			
	ChETA	0.88			
	ChRET/TC	0.56			
E_{ChR2}	**All variants**	0	mV	Reversal potential of ChR2	[61]

Table 3. Global Sensitivity Analysis Ranges for each State Variable Variance and ChR2 Parameter

	Parameter	***Range***	***Unit***
State Variable Variances	σ_{IP_3}	0 – 0.10	s$^{-1/2}$
	$\sigma_{Ca^{2+}}$	0 – 0.10	s$^{-1/2}$
	σ_h	0 – 0.10	s$^{-1/2}$
	σ_{c_o}	0 – 0.10	s$^{-1/2}$
	σ_{o_1}	0 – 0.10	s$^{-1/2}$
	σ_{o_2}	0 – 0.10	s$^{-1/2}$
	σ_{c_2}	0 – 0.10	s$^{-1/2}$
ChR2 Parameters	p_1	$51.28 – 1.50 \times 10^2$	ms^{-1}
	G_{d_1}	$8.16 – 5.47 \times 10^2$	ms^{-1}
	e_{12}	$163.52 – 1.93 \times 10^4$	ms^{-1}
	e_{21}	$4.00 – 1.31 \times 10^3$	ms^{-1}
	p_2	$14.08 – 7.70 \times 10^1$	ms^{-1}
	G_{d_2}	$56.32 – 1.81 \times 10^2$	ms^{-1}
	G_r	0.075 – 1.00	ms^{-1}
	τ_{ChR2}	0.000 – 0.0003	ms^{-1}
	γ	0.000 – 0.011	~
	g_1	0.0001 – 0.091	mS/cm^2

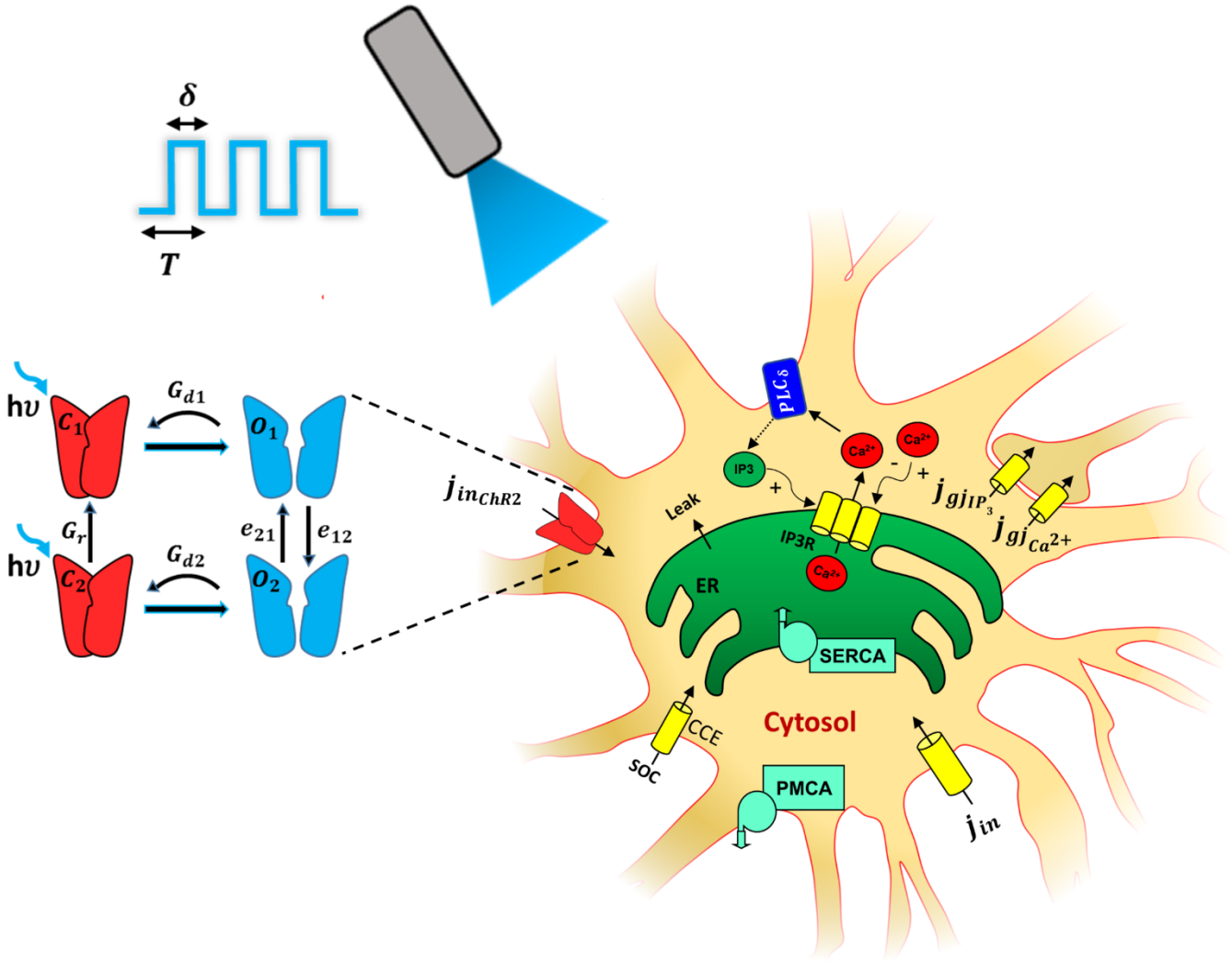

Figure 1. Schematic of the biophysical model of a ChR2 - expressing astrocyte. Inset: The 4-state model of Channelrhodopsin 2 (ChR2) – closed states (c_1 and c_2) in red, open states (o_1 and o_2) in blue. The rate constants of transitions between states are depicted in the figure. Blue light (hυ: 473nm) opens ChR2, facilitating cationic influx $j_{in_{ChR2}}$, including Ca^{2+}, initiating a cascade of Ca^{2+} responses. The light stimulation window is illustrated as a pulse train given by T (pulse period) and δ (pulse width). The model accounts for: 1) Ca^{2+} release from the endoplasmic reticulum (ER) into the cytosol via the IP_3R clusters, 2) PLCδ mediated production of IP_3, 3) capacitative calcium entry phenomenon (CCE) via the store operated calcium channel (SOC), 4) passive leak from the ER to the cytosol, 5) replenishment of ER stores via the SERCA pump, 6) extrusion of Ca^{2+} by PMCA pump (plasma membrane Ca^{2+} ATPase) into the extracellular (EC) space, and 7) passive leak (j_{in}) into the cytosol

395 from the EC. In a network of astrocytes, each cell is connected to its neighboring cells though Ca^{2+} and IP_3

396 permeable gap junctions, indicated as $j_{gj_{Ca^{2+}}}$ and $j_{gj_{IP_3}}$, respectively.

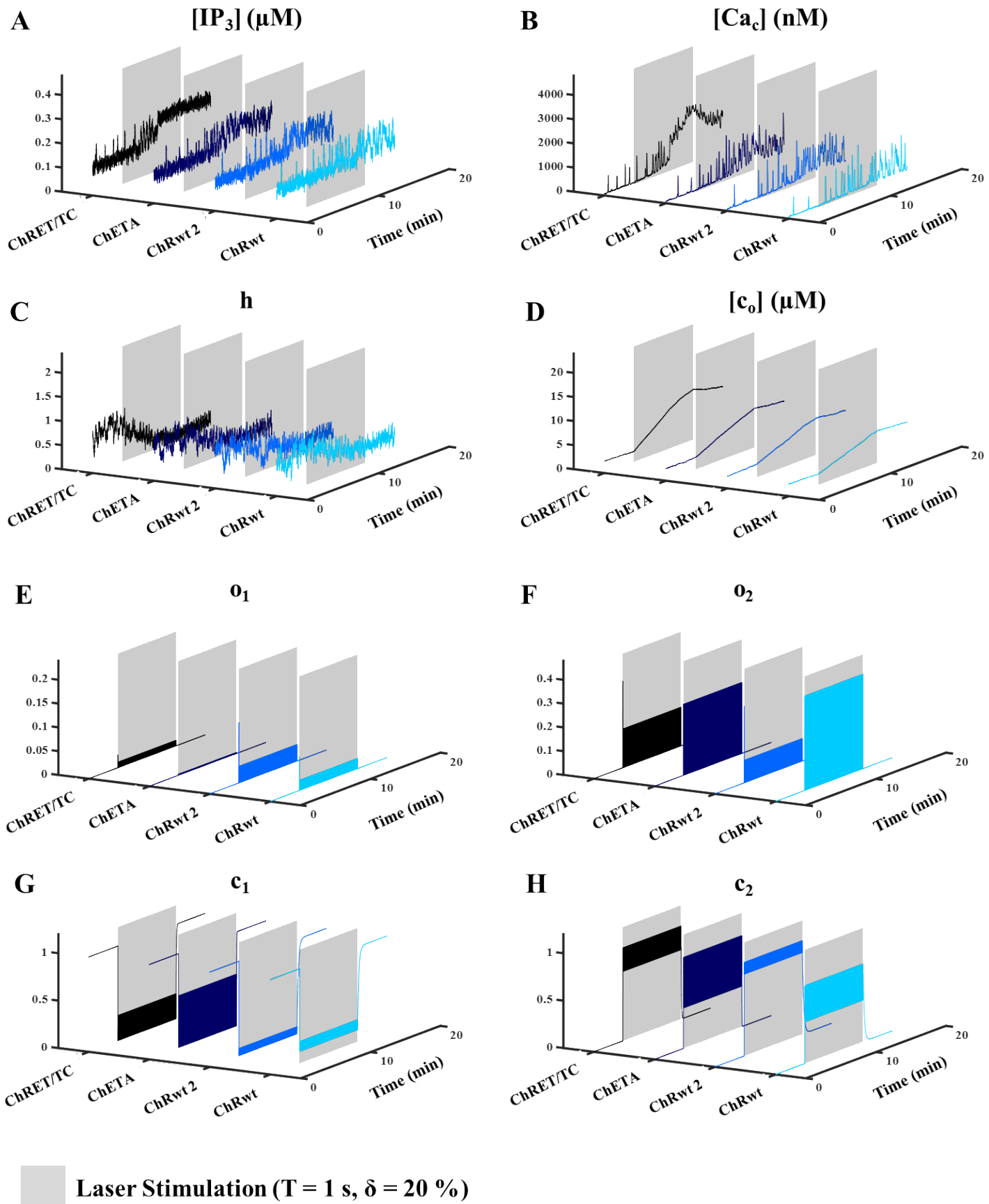

Figure 2. Response of ChR2 variants (wild type 1 (wt1), wild type 2 (wt2), ChETA and ChRET/TC) to light

stimulation. The stimulation paradigm (from 4 to 12 minutes, gray shaded region) is a pulse train with the duration (T) = 1 s, pulse width (δ) = 20% (0.2 s), and a unit pulse amplitude. **(A-D)** Representative traces of IP_3 level ($[IP_3]$), cytosolic calcium ($[Ca_c]$), inactivation IP_3R gating variable (h), and total calcium concentration ($[c_o]$) for an astrocyte expressing various ChR2 variants upon laser light stimulation are illustrated. Results show high sensitivity of all variables to light stimulation. In particular, increase in $[IP_3]$, $[Ca_c]$, and [co], and a decrease in h for all variants during light stimulation is observed. $[Ca_c]$ traces for the ChRET/TC variant during stimulation shows an elevation of calcium beyond physiological levels, and an apparent reduction in the calcium spiking activity compared to other variants shown in panel B. **(E-H)** Representative traces of the open (o_1, o_2) and closed states of ChR2 (c_1, c_2) are plotted with respect to time (min), for an astrocyte expressing different variants of ChR2. During pre and post light stimulation phases, all variants have the tendency to stay in the c_1 state. During the period of stimulus, however, variants show varying degrees of existence in all open and closed states of ChR2.

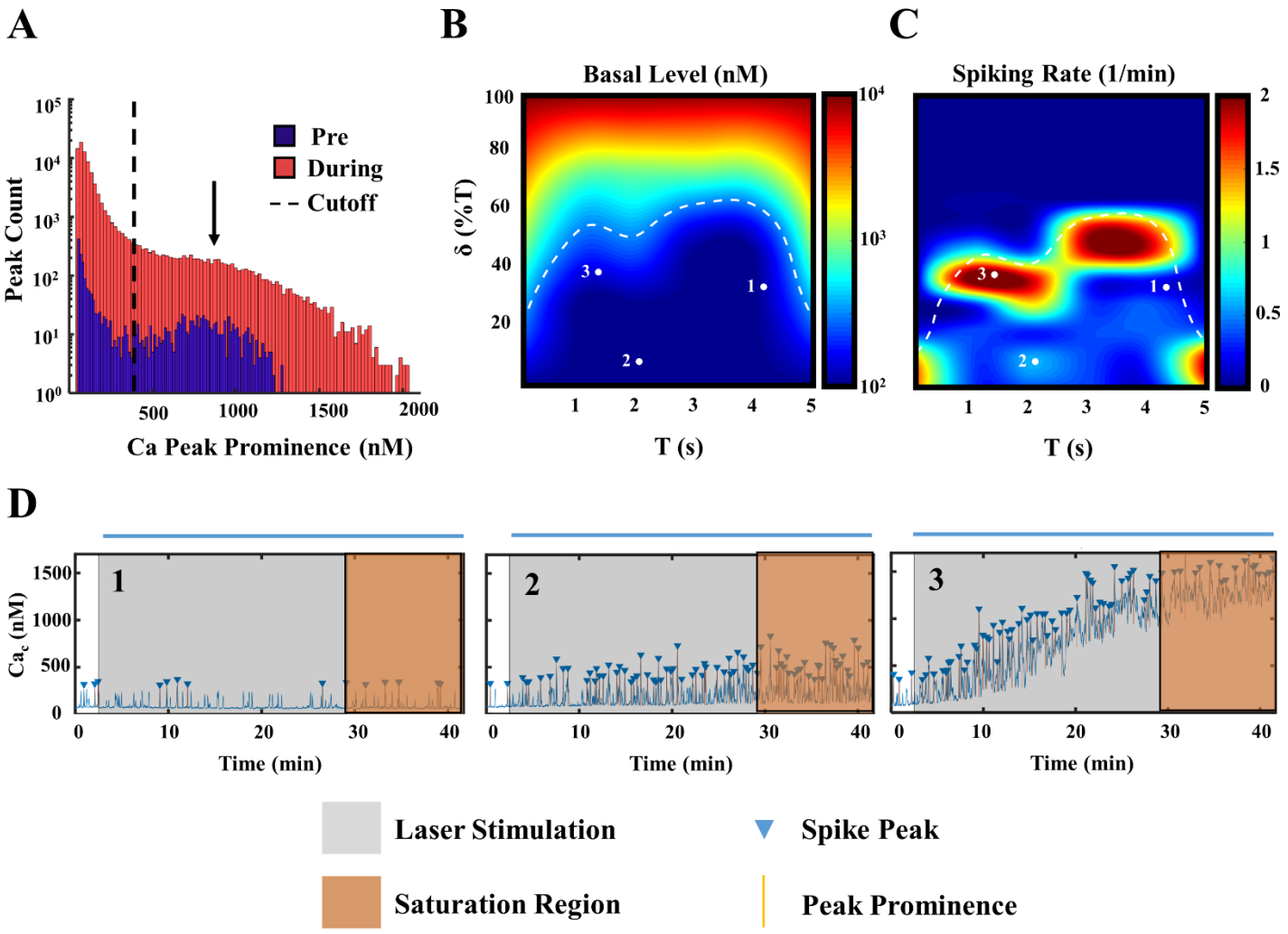

Figure 3. Response of a ChETA - expressing astrocyte to various light stimulation paradigms. A. Histogram depicting the peak count in the Ca^{2+} trace of the astrocyte (log scale) with respect to Ca^{2+} peak prominence upon laser light stimulation. Light stimulation parameters – T was varied between 1-5 s; δ between 0-100% of T; unit pulse amplitude. The histogram was generated for the pre-stimulus phase (blue) and during stimulus phase (red). The cutoff prominence was set to 350 nM, in accordance with the observed bimodal distribution of Ca^{2+} spikes (dashed line), and to assure that 1/f noise related Ca^{2+} spikes are not included in the analysis. **B.** The T-δ heat map of the Ca^{2+} basal level for various combinatorial windows of T and δ, expressed in the log scale. Specific regions in the physiological levels of Ca^{2+} basal level (indicated by the white dashed trace) are numbered and used for further plotting and analysis. **C.** The T-δ heat map indicating spiking rate in the astrocyte for various combinatorial windows of T and δ, above the cutoff prominence chosen in (**A**). White dashed trace delimits the physiological

basal levels; as defined in (**B**). **D.** Representative Ca^{2+} signaling traces of points 1, 2 and 3, from (**B**) and (**C**). Light stimulation was started at 50 s until the end of the simulation (blue bar). Mean Ca^{2+} spiking rate across trials was calculated once the Ca^{2+} signal trace reached a steady profile (in orange).

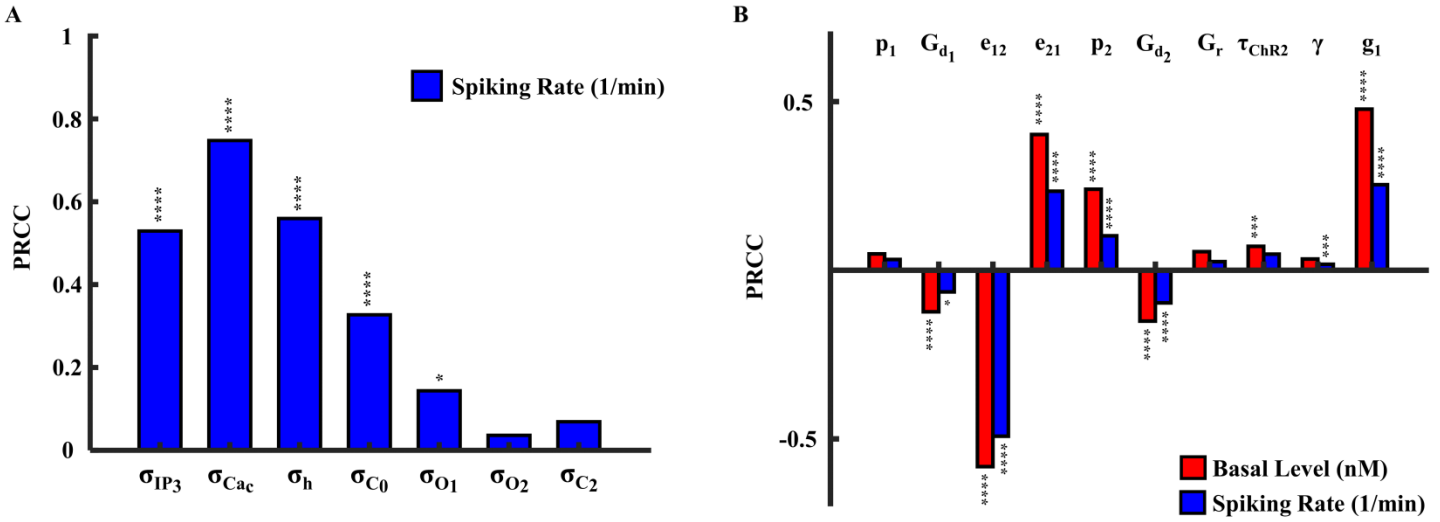

Figure 4. Sensitivity of the astrocytic Ca^{2+} response to the state variable variances and ChR2 parameters. **A.** Global sensitivity analysis results depicting sensitivity of astrocyte Ca^{2+} response to stochastic noises, without light stimulation. Partial rank correlation coefficients (PRCCs) with respect to the Weiner processes of the state variables are plotted. 500 parameter sets chosen by the Latin hypercube sampling (LHS) method with uniform distribution. * depicts significance levels. Spiking rate *p*-values: $\sigma_{IP_3} = 1.3 \times 10^{-22}$; $\sigma_{Ca_c} = 8.9 \times 10^{-54}$; $\sigma_h = 1.4 \times 10^{-25}$; $\sigma_{c_o} = 9.5 \times 10^{-9}$; $\sigma_{o_1} = 0.014$. **B.** Plot of the PRCCs for each parameter of ChR2 during light stimulation (T= 4.5 s, δ = 1.35 s (30% of T), light stimulation started at 50 s and continued for the duration of the simulation, (total simulation time = 40 min, 10 trials) with respect to the basal level (nM) and spiking rate (1/min); peak prominence = 350 nM. 1000 parameter sets were chosen using the LHS sampling method with uniform distribution. Spiking rate p-values: $G_{d1} = 0.016(*)$; $e_{12}{\sim}0$; $e_{21}{\sim}0$; $p_2{\sim}0$; $G_{d2} = 5 \times 10^{-7}(****)$; $\gamma = 0.004(***)$; $g_1{\sim}0\ (****)$. Basal level p-values: $G_{d1} = 0.001(***)$; $e_{12}{\sim}0$; $e_{21}{\sim}0$; $p_2 = 3.1 \times 10^{-14}$ $(****)$; $G_{d2} = 2.3 \times 10^{-6}(****)$; $\tau_{ChR2} = 0.027(***)$; $g_1{\sim}0\ (****)$.

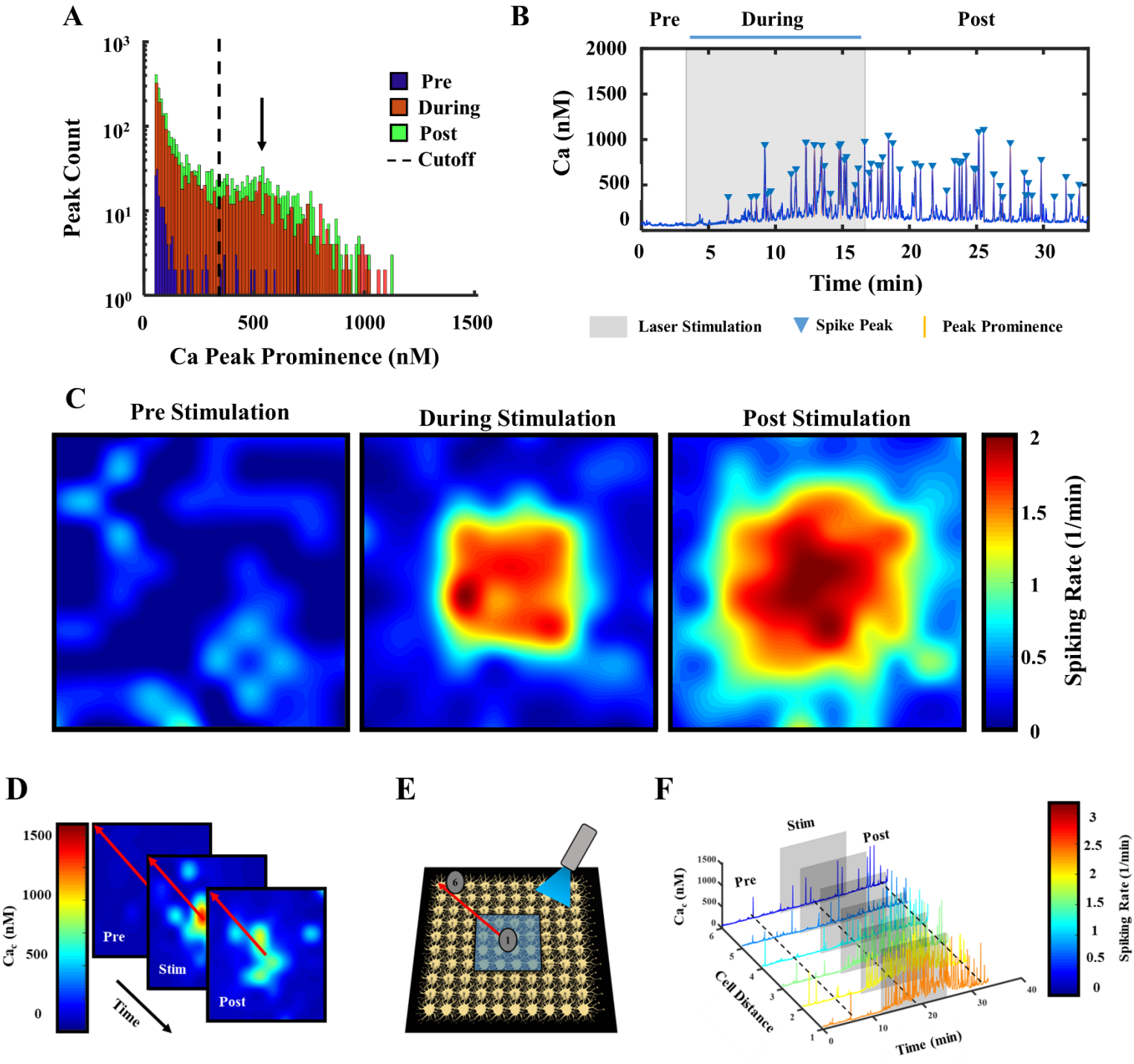

Figure 5. Network-wide behavior of astrocytic Ca^{2+} responses to light stimulation. A. Histogram (log scale) depicting the peak count in the Ca^{2+} traces in a 10 x 10 network (100 astrocytes) homogenously expressing ChETA with respect to the Ca^{2+} peak prominence during the pre-stimulus (blue), during stimulus (red) and post stimulus (green) phases. Light stimulation parameters – T = 2 s; δ =15%; unit pulse amplitude. The cutoff peak prominence was set to 350 nM (dashed line) due to the bimodal distribution of Ca^{2+} spikes and assures that 1/f

related irrelevant Ca^{2+} spikes are excluded from the analysis. **B.** A representative trace showing the Ca^{2+} signaling profile over time. Light stimulation was performed between 12 – 25 min. (grey shaded region, blue bar). **C.** Heat map indicating the mean Ca^{2+} spiking rate above the cutoff prominence (indicated in (**A**) in the network - pre, during and post light stimulation. **D.** Heat map indicating the Ca^{2+} basal levels in the network – pre, during and post light stimulation. Astrocytes oriented across a diagonal (indicated by red line) were used for further interpretation in (**F**). **E.** Illustration of 4 x 4 subnetwork of astrocytes focally stimulated by blue laser light (indicated by the blue shaded region). 6 astrocytes across the diagonal (in the direction of the red arrow), were used to evaluate the effect of distance from the stimulation on cytosolic Ca^{2+} profiles. **F.** Depiction of Ca^{2+} signal profiles of these 6 astrocytes (in **E**), plotted as a function of time; light stimulation window in grey, color bar represents the mean spiking rate.

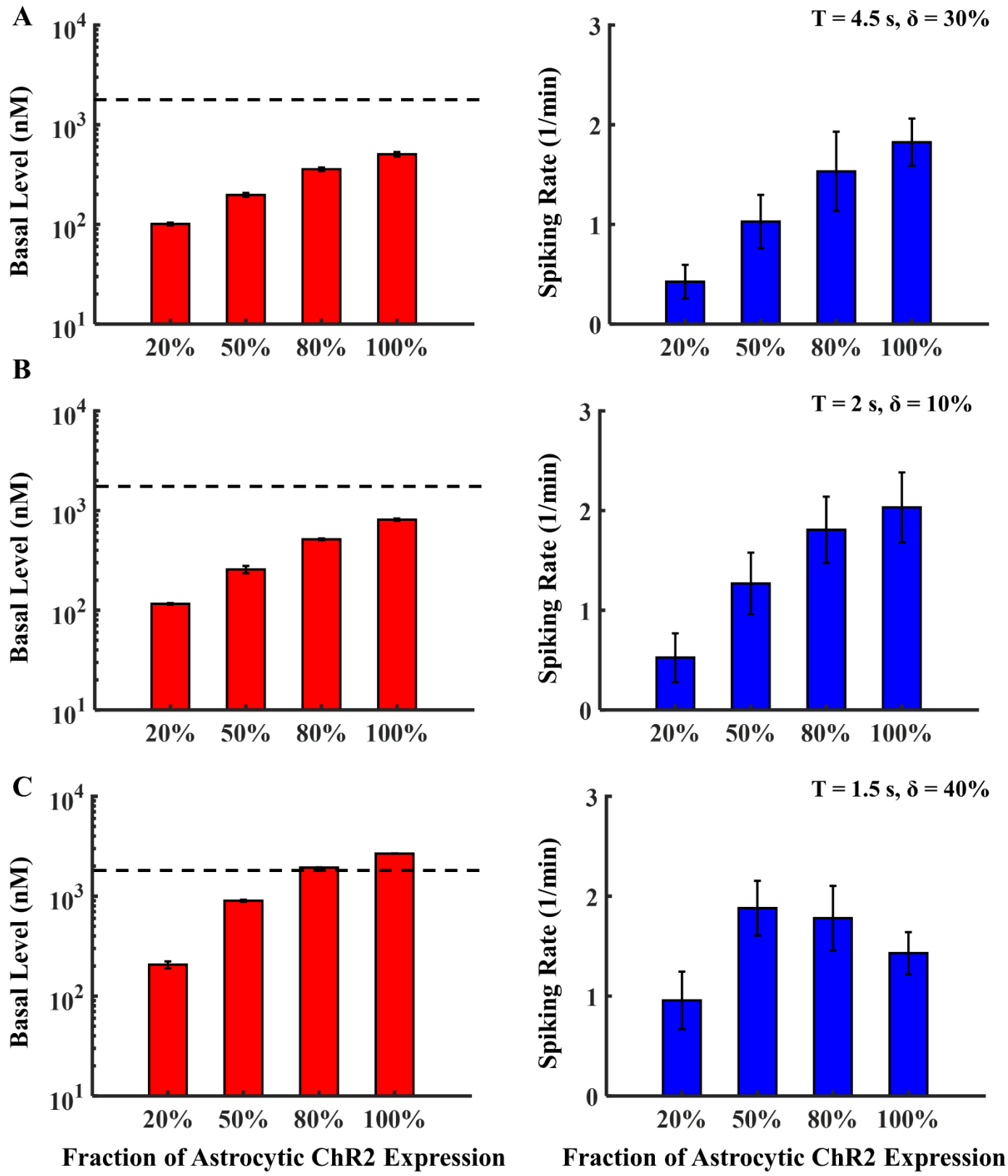

484 **Figure 6. Effect of ChETA expression heterogeneity on network-wide light stimulation.** Each bar chart shows
485 the mean network basal level (nM) and spiking rate (1/min) as a function of astrocyte ChR2 expression fraction.

Each part corresponds to network-wide stimulation with 1 of 3 different paradigms: **A.** point 1 of Figure 3 (T = 4.5 s, δ = 1.35 s (30% of T), low Ca^{2+} activity), **B.** point 2 of Fig. 3 (T = 2 s, δ = 0.2 s (10% of T), intermediate Ca^{2+} activity), and **C.** point 3 of Figure 3 (T = 1.5 s, δ = 0.6 s (40% of T), high Ca^{2+} activity). In all 3 cases, the stimulation was initiated at 50 s and continued for the duration of the simulation, and the black dashed line marks the maximum physiological basal level of astrocytes.

Supplementary Figures -Effect of light stimulation on different ChR2 variants

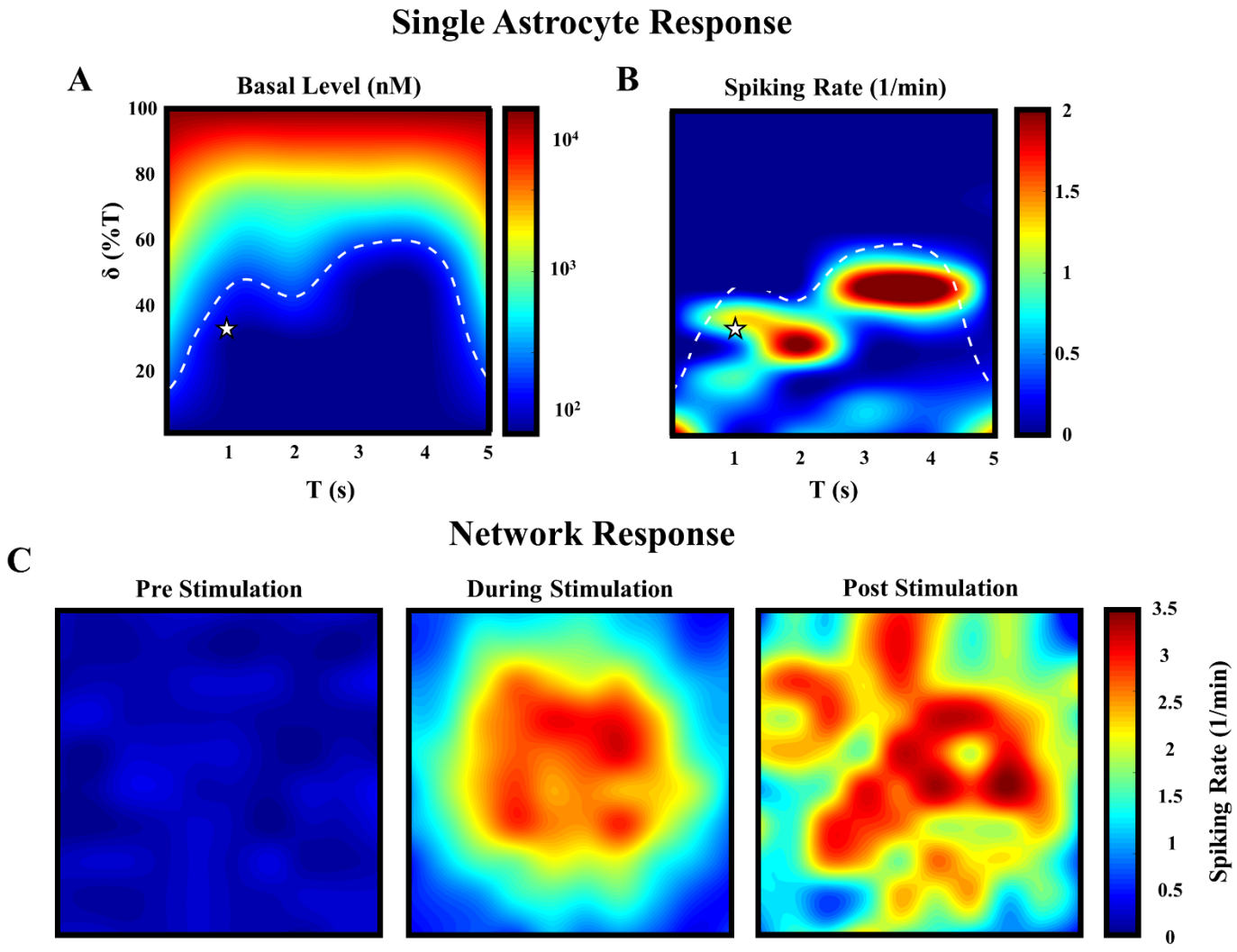

Figure S1. Response of ChRET/TC - expressing astrocytes to light stimulation A. Heat map of the Ca^{2+} steady state basal level for various combinatorial windows of time duration (T) and pulse widths (δ; expressed as a percentage of T), expressed in the log scale. The physiological levels of Ca^{2+} basal level are indicated by the white dashed line. **B.** Heat map indicating spiking rate in the astrocyte for various combinatorial windows of T and δ, above the cutoff prominence chosen in Figure 3A. **C.** Heat maps indicating the mean spiking rate of astrocytes in the network - pre, during and post light stimulation (T = 1 s, δ = 0.3 s (30% of T), the point denoted by star in **A** and **B**.

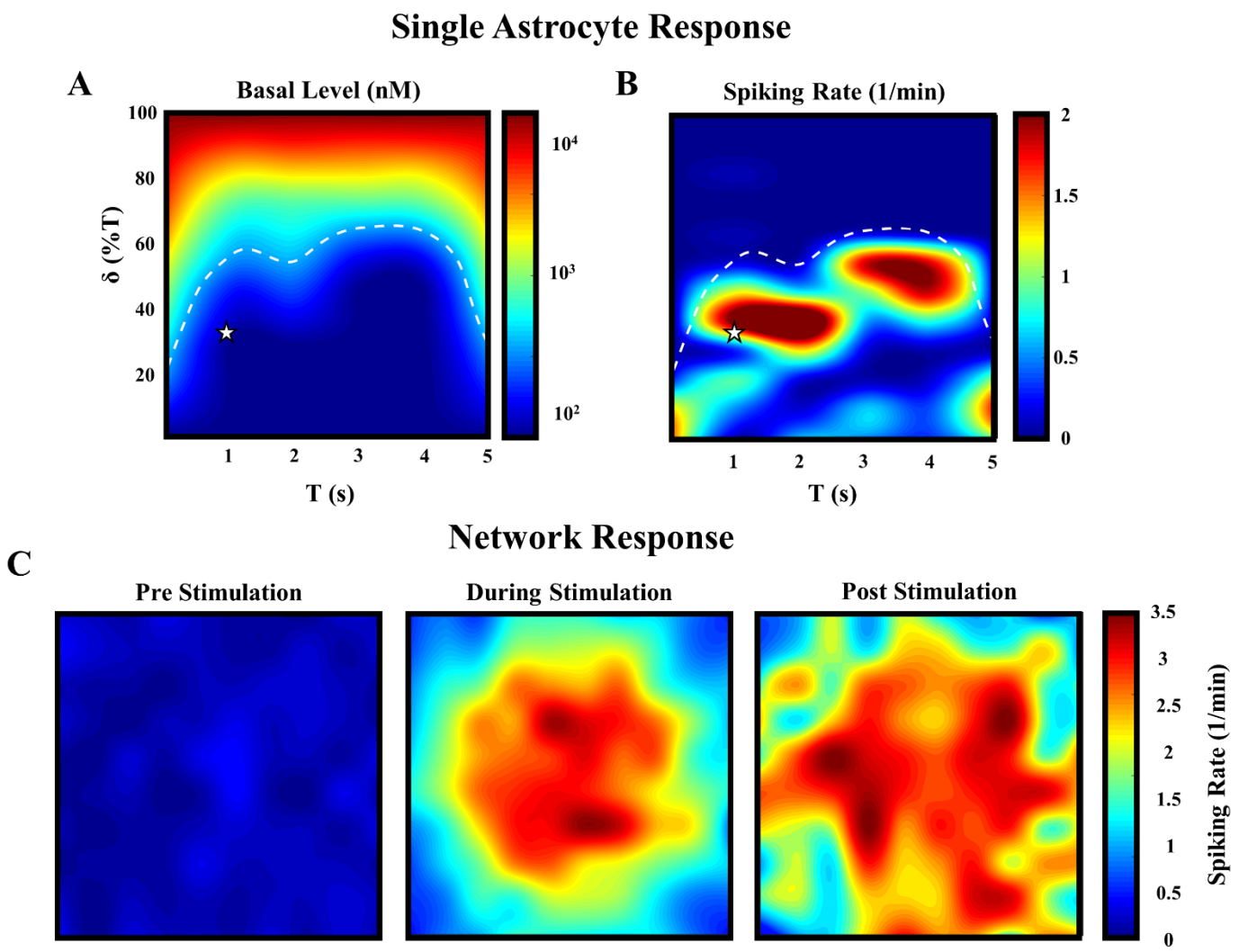

Figure S2. Response of ChRwt1 - expressing astrocytes to light stimulation. A. Heat map of the Ca^{2+} steady state basal level for various combinatorial windows of time duration (T) and pulse widths (δ; expressed as a percentage of T), expressed in the log scale. The physiological levels of Ca^{2+} basal level are indicated by the white dashed line. **B.** Heat map indicating spiking rate in the astrocyte for various combinatorial windows of T and δ, above the cutoff prominence chosen in Figure 3A. **C.** Heat maps indicating the mean spiking rate of astrocytes in the network - pre, during and post light stimulation (T = 1 s, δ = 0.3 s (30% of T), the point denoted by star in **A** and **B**.

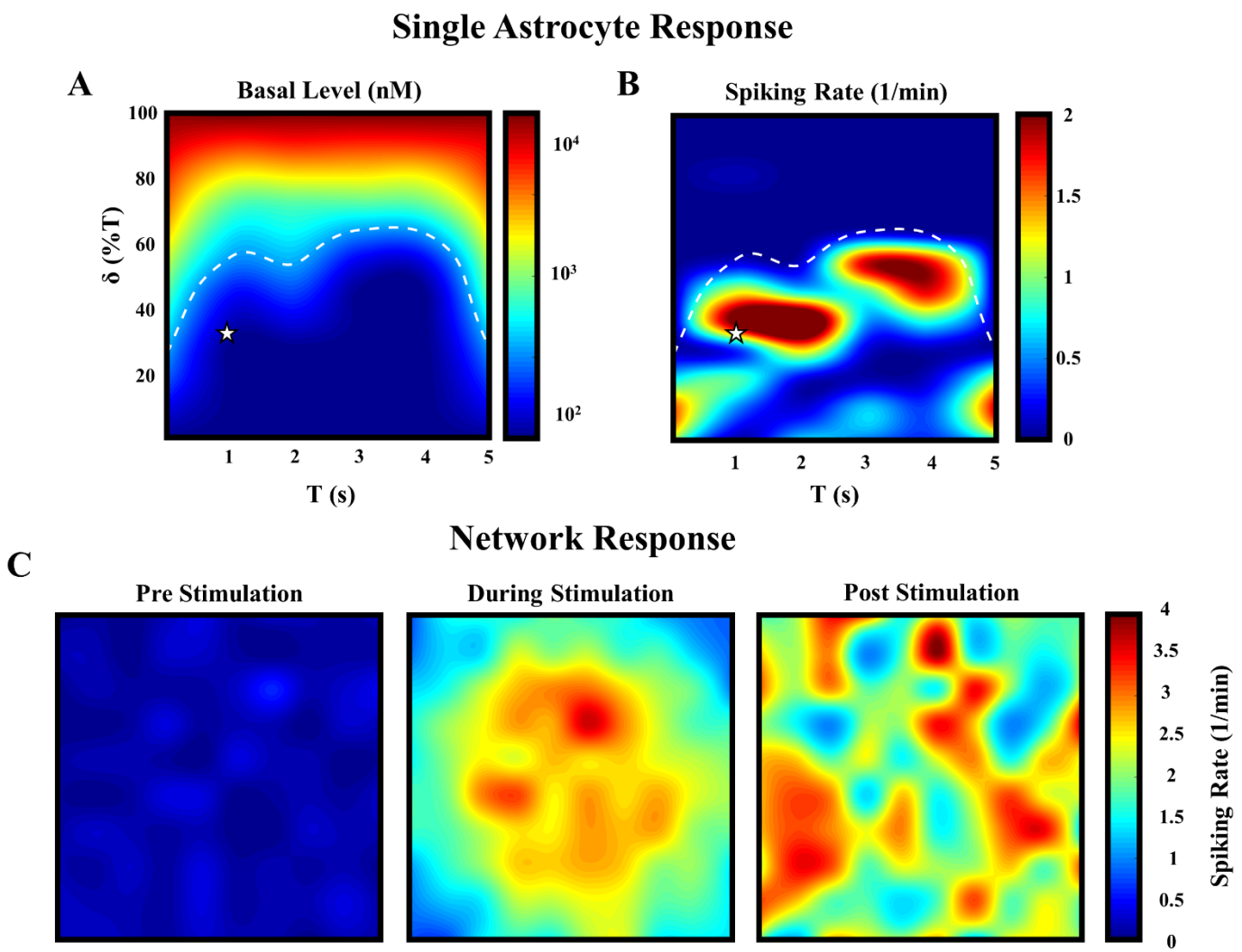

Figure S3. Response of ChRwt2 - expressing astrocytes to light stimulation. A. Heat map of the Ca^{2+} final basal level for various combinatorial windows of time duration (T) and pulse widths (δ; expressed as a percentage of T), expressed in the log scale. The physiological levels of Ca^{2+} basal level are indicated by the white dashed line. **B.** Heat map indicating spiking rate in the astrocyte for various combinatorial windows of T and δ, above the cutoff prominence chosen in Figure 3A. **C.** Heat maps indicating the mean spiking rate of astrocytes in the network - pre, during and post light stimulation (T = 1 s, δ = 0.3 s (30% of T), point denoted by star in **A** and **B**.

Video S1. Movie of complete network-wide behavior of astrocytes to light stimulation. In this video the stimulation window is marked in red. Parameters and stimulation specifics are as in Figure 5.

Bibliography

1. Carmignoto G, Gómez-Gonzalo M. The contribution of astrocyte signalling to neurovascular coupling. Brain research reviews. 2010;63(1-2):138-48.
2. Riera JJ, Sumiyoshi A. Brain oscillations: ideal scenery to understand the neurovascular coupling. Current opinion in neurology. 2010;23(4):374-81.
3. Zonta M, Angulo MC, Gobbo S, Rosengarten B, Hossmann K-A, Pozzan T, et al. Neuron-to-astrocyte signaling is central to the dynamic control of brain microcirculation. Nature neuroscience. 2003;6(1):43.
4. Araque A, Parpura V, Sanzgiri RP, Haydon PG. Glutamate-dependent astrocyte modulation of synaptic transmission between cultured hippocampal neurons. European Journal of Neuroscience. 1998;10(6):2129-42.
5. Volterra A, Meldolesi J. Astrocytes, from brain glue to communication elements: the revolution continues. Nature Reviews Neuroscience. 2005;6(8):626.
6. Zorec R, Araque A, Carmignoto G, Haydon PG, Verkhratsky A, Parpura V. Astroglial excitability and gliotransmission: an appraisal of Ca2+ as a signalling route. ASN neuro. 2012;4(2):AN20110061.
7. Magistretti PJ. Neuron–glia metabolic coupling and plasticity. Experimental physiology. 2011;96(4):407-10.
8. Smith SJ. Neural signalling: Neuromodulatory astrocytes. Current Biology. 1994;4(9):807-10.
9. Riera JJ, Schousboe A, Waagepetersen HS, Howarth C, Hyder F. The micro-architecture of the cerebral cortex: functional neuroimaging models and metabolism. Neuroimage. 2008;40(4):1436-59.
10. Devinsky O, Vezzani A, Najjar S, De Lanerolle NC, Rogawski MA. Glia and epilepsy: excitability and inflammation. Trends in neurosciences. 2013;36(3):174-84.
11. Agulhon C, Sun M-Y, Murphy T, Myers T, Lauderdale K, Fiacco TA. Calcium signaling and gliotransmission in normal vs. reactive astrocytes. Frontiers in pharmacology. 2012;3:139.
12. Hanisch UK. Microglia as a source and target of cytokines. Glia. 2002;40(2):140-55.
13. Vezzani A, Friedman A, Dingledine RJ. The role of inflammation in epileptogenesis. Neuropharmacology. 2013;69:16-24.
14. Eid T, Tu N, Lee T-SW, Lai JC. Regulation of astrocyte glutamine synthetase in epilepsy. Neurochemistry international. 2013;63(7):670-81.

15. Girouard H, Iadecola C. Neurovascular coupling in the normal brain and in hypertension, stroke, and Alzheimer disease. Journal of applied physiology. 2006;100(1):328-35.
16. Losi G, Cammarota M, Carmignoto G. The role of astroglia in the epileptic brain. Frontiers in pharmacology. 2012;3:132.
17. Seifert G, Carmignoto G, Steinhäuser C. Astrocyte dysfunction in epilepsy. Brain research reviews. 2010;63(1-2):212-21.
18. Sidoryk-Wegrzynowicz M, Wegrzynowicz M, Lee E, Bowman AB, Aschner M. Role of astrocytes in brain function and disease. Toxicologic pathology. 2011;39(1):115-23.
19. Verkhratsky A, Steardo L, Parpura V, Montana V. Translational potential of astrocytes in brain disorders. Progress in neurobiology. 2016;144:188-205.
20. Wetherington J, Serrano G, Dingledine R. Astrocytes in the epileptic brain. Neuron. 2008;58(2):168-78.
21. Berridge MJ. Elementary and global aspects of calcium signalling. The Journal of physiology. 1997;499(2):291-306.
22. Cornell-Bell AH, Finkbeiner SM, Cooper MS, Smith SJ. Glutamate induces calcium waves in cultured astrocytes: long-range glial signaling. Science. 1990;247(4941):470-3.
23. De Pittà M, Volman V, Berry H, Parpura V, Volterra A, Ben-Jacob E. Computational quest for understanding the role of astrocyte signaling in synaptic transmission and plasticity. Frontiers in computational neuroscience. 2012;6:98.
24. Fujii Y, Maekawa S, Morita M. Astrocyte calcium waves propagate proximally by gap junction and distally by extracellular diffusion of ATP released from volume-regulated anion channels. Scientific reports. 2017;7(1):13115.
25. Laskey AD, Roth BJ, Simpson PB, Russell JT. Images of Ca2+ flux in astrocytes: evidence for spatially distinct sites of Ca2+ release and uptake. Cell Calcium. 1998;23(6):423-32.
26. Araque A, Parpura V, Sanzgiri RP, Haydon PG. Tripartite synapses: glia, the unacknowledged partner. Trends in neurosciences. 1999;22(5):208-15.
27. Fleischer W, Theiss S, Slotta J, Holland C, Schnitzler A. High-frequency voltage oscillations in cultured astrocytes. Physiological reports. 2015;3(5).
28. Hassinger T, Guthrie P, Atkinson P, Bennett M, Kater S. An extracellular signaling component in propagation of astrocytic calcium waves. Proceedings of the National Academy of Sciences. 1996;93(23):13268-73.

29. Nedergaard M, Cooper AJ, Goldman SA. Gap junctions are required for the propagation of spreading depression. Journal of neurobiology. 1995;28(4):433-44.

30. Charles AC, Merrill JE, Dirksen ER, Sandersont MJ. Intercellular signaling in glial cells: calcium waves and oscillations in response to mechanical stimulation and glutamate. Neuron. 1991;6(6):983-92.

31. Guthrie PB, Knappenberger J, Segal M, Bennett MV, Charles AC, Kater SB. ATP released from astrocytes mediates glial calcium waves. Journal of Neuroscience. 1999;19(2):520-8.

32. Stout CE, Costantin JL, Naus CC, Charles AC. Intercellular calcium signaling in astrocytes via ATP release through connexin hemichannels. Journal of Biological Chemistry. 2002;277(12):10482-8.

33. Parpura V, Basarsky TA, Liu F, Jeftinija K, Jeftinija S, Haydon PG. Glutamate-mediated astrocyte–neuron signalling. Nature. 1994;369(6483):744.

34. Jeremic A, Jeftinija K, Stevanovic J, Glavaski A, Jeftinija S. ATP stimulates calcium-dependent glutamate release from cultured astrocytes. Journal of neurochemistry. 2001;77(2):664-75.

35. Ellis E, McKinney J, Willoughby K, Liang S, Povlishock J. A new model for rapid stretch-induced injury of cells in culture: characterization of the model using astrocytes. Journal of neurotrauma. 1995;12(3):325-39.

36. Choi JW, Gardell SE, Herr DR, Rivera R, Lee C-W, Noguchi K, et al. FTY720 (fingolimod) efficacy in an animal model of multiple sclerosis requires astrocyte sphingosine 1-phosphate receptor 1 (S1P1) modulation. Proceedings of the National Academy of Sciences. 2011;108(2):751-6.

37. Fenno L, Yizhar O, Deisseroth K. The development and application of optogenetics. Annual review of neuroscience. 2011;34.

38. Mascaro ALA, Silvestri L, Sacconi L, Pavone FS. Breakthroughs in Photonics 2012: Nonlinear Laser Imaging for Neuroscience. IEEE Photonics Journal. 2013;5(2):0701006-.

39. Mohanty SK, Lakshminarayananan V. Optical techniques in optogenetics. Journal of modern optics. 2015;62(12):949-70.

40. Vaziri A, Emiliani V. Reshaping the optical dimension in optogenetics. Current opinion in neurobiology. 2012;22(1):128-37.

41. Adamantidis AR, Zhang F, de Lecea L, Deisseroth K. Optogenetics: opsins and optical interfaces in neuroscience. Cold Spring Harbor Protocols. 2014;2014(8):pdb. top083329.

42. Deisseroth K. Optogenetics: 10 years of microbial opsins in neuroscience. Nature neuroscience. 2015;18(9):1213.

43. Krook-Magnuson E, Ledri M, Soltesz I, Kokaia M. How might novel technologies such as optogenetics lead to better treatments in epilepsy? Issues in Clinical Epileptology: A View from the Bench: Springer; 2014. p. 319-36.

44. Berndt A, Schoenenberger P, Mattis J, Tye KM, Deisseroth K, Hegemann P, et al. High-efficiency channelrhodopsins for fast neuronal stimulation at low light levels. Proceedings of the National Academy of Sciences. 2011;108(18):7595-600.

45. Lin JY. A user's guide to channelrhodopsin variants: features, limitations and future developments. Experimental physiology. 2011;96(1):19-25.

46. Lin JY. Optogenetic excitation of neurons with channelrhodopsins: light instrumentation, expression systems, and channelrhodopsin variants. Progress in brain research. 196: Elsevier; 2012. p. 29-47.

47. Lin JY, Lin MZ, Steinbach P, Tsien RY. Characterization of engineered channelrhodopsin variants with improved properties and kinetics. Biophysical journal. 2009;96(5):1803-14.

48. Gunaydin LA, Yizhar O, Berndt A, Sohal VS, Deisseroth K, Hegemann P. Ultrafast optogenetic control. Nature neuroscience. 2010;13(3):387.

49. Prigge M, Schneider F, Tsunoda SP, Shilyansky C, Wietek J, Deisseroth K, et al. Color-tuned channelrhodopsins for multiwavelength optogenetics. Journal of Biological Chemistry. 2012:jbc. M112. 391185.

50. Figueiredo á, Lane S, Tang F, Liu B, Hewinson J, Marina N, et al. Optogenetic experimentation on astrocytes. Experimental physiology. 2011;96(1):40-50.

51. Figueiredo M, Lane S, Stout Jr RF, Liu B, Parpura V, Teschemacher AG, et al. Comparative analysis of optogenetic actuators in cultured astrocytes. Cell Calcium. 2014;56(3):208-14.

52. Gradinaru V, Mogri M, Thompson KR, Henderson JM, Deisseroth K. Optical deconstruction of parkinsonian neural circuitry. science. 2009;324(5925):354-9.

53. Masamoto K, Unekawa M, Watanabe T, Toriumi H, Takuwa H, Kawaguchi H, et al. Unveiling astrocytic control of cerebral blood flow with optogenetics. Scientific reports. 2015;5:11455.

54. Takata N, Sugiura Y, Yoshida K, Koizumi M, Hiroshi N, Honda K, et al. Optogenetic astrocyte activation evokes BOLD fMRI response with oxygen consumption without neuronal activity modulation. Glia. 2018.

639 55. Adamsky A, Kol A, Kreisel T, Doron A, Ozeri-Engelhard N, Melcer T, et al. Astrocytic Activation Generates De
640 Novo Neuronal Potentiation and Memory Enhancement. Cell. 2018.
641 56. Poskanzer KE, Yuste R. Astrocytes regulate cortical state switching in vivo. Proceedings of the National Academy of
642 Sciences. 2016;113(19):E2675-E84.
643 57. Ding X, Zhang X, Ji L. Contribution of calcium fluxes to astrocyte spontaneous calcium oscillations in deterministic
644 and stochastic models. Applied Mathematical Modelling. 2018;55:371-82.
645 58. Riera J, Hatanaka R, Uchida T, Ozaki T, Kawashima R. Quantifying the uncertainty of spontaneous Ca 2+ oscillations
646 in astrocytes: particulars of Alzheimer's disease. Biophysical journal. 2011;101(3):554-64.
647 59. Riera J, Hatanaka R, Ozaki T, Kawashima R. Modeling the spontaneous Ca2+ oscillations in astrocytes:
648 inconsistencies and usefulness. Journal of integrative neuroscience. 2011;10(04):439-73.
649 60. Stefanescu RA, Shivakeshavan R, Khargonekar PP, Talathi SS. Computational modeling of channelrhodopsin-2
650 photocurrent characteristics in relation to neural signaling. Bulletin of mathematical biology. 2013;75(11):2208-40.
651 61. Williams JC, Xu J, Lu Z, Klimas A, Chen X, Ambrosi CM, et al. Computational optogenetics: empirically-derived
652 voltage-and light-sensitive channelrhodopsin-2 model. PLoS computational biology. 2013;9(9):e1003220.
653 62. De Young GW, Keizer J. A single-pool inositol 1, 4, 5-trisphosphate-receptor-based model for agonist-stimulated
654 oscillations in Ca2+ concentration. Proceedings of the National Academy of Sciences. 1992;89(20):9895-9.
655 63. Li Y-X, Rinzel J. Equations for InsP3 receptor-mediated [Ca2+] i oscillations derived from a detailed kinetic model: a
656 Hodgkin-Huxley like formalism. Journal of theoretical Biology. 1994;166(4):461-73.
657 64. Shuai J-W, Jung P. Stochastic properties of Ca2+ release of inositol 1, 4, 5-trisphosphate receptor clusters.
658 Biophysical journal. 2002;83(1):87-97.
659 65. Ozaki T. A local linearization approach to nonlinear filtering. International Journal of Control. 1993;57(1):75-96.
660 66. Marino S, Hogue IB, Ray CJ, Kirschner DE. A methodology for performing global uncertainty and sensitivity
661 analysis in systems biology. Journal of theoretical biology. 2008;254(1):178-96.
662 67. McKay MD, Beckman RJ, Conover WJ. Comparison of three methods for selecting values of input variables in the
663 analysis of output from a computer code. Technometrics. 1979;21(2):239-45.

68. Hermonat PL, Muzyczka N. Use of adeno-associated virus as a mammalian DNA cloning vector: transduction of neomycin resistance into mammalian tissue culture cells. Proceedings of the National Academy of Sciences. 1984;81(20):6466-70.

69. McCown TJ, Xiao X, Li J, Breese GR, Samulski RJ. Differential and persistent expression patterns of CNS gene transfer by an adeno-associated virus (AAV) vector. Brain research. 1996;713(1-2):99-107.

70. Savtchenko LP, Bard L, Jensen TP, Reynolds JP, Kraev I, Medvedev N, et al. Disentangling astroglial physiology with a realistic cell model in silico. Nature communications. 2018;9(1):3554.

71. Lallouette J, De Pittà M, Berry H. Astrocyte networks and intercellular calcium propagation. Computational Glioscience: Springer; 2019. p. 177-210.

72. Fink CC, Slepchenko B, Loew LM. Determination of time-dependent inositol-1, 4, 5-trisphosphate concentrations during calcium release in a smooth muscle cell. Biophysical journal. 1999;77(1):617-28.

73. Di Garbo A, Barbi M, Chillemi S, Alloisio S, Nobile M. Calcium signalling in astrocytes and modulation of neural activity. Biosystems. 2007;89(1-3):74-83.

74. Stamatakis M, Mantzaris NV. Modeling of ATP-mediated signal transduction and wave propagation in astrocytic cellular networks. Journal of theoretical biology. 2006;241(3):649-68.

75. Lavrentovich M, Hemkin S. A mathematical model of spontaneous calcium (II) oscillations in astrocytes. Journal of Theoretical Biology. 2008;251(4):553-60.

76. Zeng S, Li B, Zeng S, Chen S. Simulation of spontaneous Ca2+ oscillations in astrocytes mediated by voltage-gated calcium channels. Biophysical journal. 2009;97(9):2429-37.

77. Ullah G, Jung P, Cornell-Bell AH. Anti-phase calcium oscillations in astrocytes via inositol (1, 4, 5)-trisphosphate regeneration. Cell calcium. 2006;39(3):197-208.

78. Williams V, Grossman R, Edmunds SM. Volume and surface area estimates of astrocytes in the sensorimotor cortex of the cat. Neuroscience. 1980;5(7):1151-9.